# Room-Temperature Ferromagnetism in Ni(II)-Chromia based Core-Shell Nanoparticles: Experiment and First Principles Calculations

| | |
|---|---|
| Journal: | *Physical Chemistry Chemical Physics* |
| Manuscript ID | CP-ART-12-2017-008597.R1 |
| Article Type: | Paper |
| Date Submitted by the Author: | 07-Mar-2018 |
| Complete List of Authors: | Hossain, Mohammad Delower; Missouri State University, PAMS<br>Mayanovic, Robert; Missouri State University, Department of Physics, Astronomy & Materials Science<br>Dey, Sonal; SUNY Polytechnic Institute, Colleges of Nanoscale Science and Engineering<br>Sakidja, Ridwan; Missouri State University, Physics, Astronomy and Materials Science<br>Benamara, Mourad; University of Arkansas, Physics |
| | |

Journal Name

ARTICLE

# Room-Temperature Ferromagnetism in Ni(II)-Chromia based Core-Shell Nanoparticles: Experiment and First Principles Calculations

Received 00th January 20xx,
Accepted 00th January 20xx

DOI: 10.1039/x0xx00000x

**www.rsc.org/**

M.D. Hossain,[a] R.A. Mayanovic,[a,†] S. Dey,[a,§] R. Sakidja,[a] and M. Benamara[c]

We have synthesized bimagnetic core-shell nanoparticles containing a first-of-its-kind Ni(II)-chromia nanophase shell and a well-defined, epitaxial core-shell interface. Magnetic measurements reveal a substantial coercivity of the nanoparticles and a significant exchange bias effect between the antiferromagnetic chromia core and the ferromagnetic Ni(II)-chromia shell at low temperatures. The ferromagnetism and a weak exchange bias effect are found to persist to room temperature in the core-shell nanoparticles of ~ 57 nm average size. Our first principles Density Functional Theory (DFT) calculations confirm that the novel corundum-structued Ni(II)-chromia phase has an equilibrium cluster-localized ferromagnetic spin configuration. In addition, the DFT-based calculations show that the Ni(II)-chromia phase is a Mott-Hubbard insulator, with a narrowed energy band gap and increased covalent bonding due to strong hybridization between Ni 3d and O 2p levels in the upper portion of the valence band and within the band gap region. The antiferromagnetic, ferromagnetic and magnetoelectric properties of our core-shell nanoparticles make these well suited for patterned recording media and biomedical applications.

## Introduction

Due to their composite nature, core-shell nanoparticles (CSNs) offer a high degree of tunability of the magnetic and other physicochemical properties through the adjustment of core and shell size, morphology, chemical content, and structure at the atomic scale. In addition, their composite architecture often adds multifunctionality to CSNs, leading to a wide variety of potential applications, including in energy storage and harvesting, hetero- and photocatalysis, magnetic devices, photonics, and biomedicine.[1–6] In particular, bimagnetic core-shell nanoparticles are currently attracting considerable attention because their enhanced magnetic properties are highly promising for potential applications in magnetic random access memory and spintronic devices, cell separation, tissue engineering, drug delivery, MRI targeted-cell imaging, and hyperthermia.[7–9] Conventional bimagnetic CSNs have a ferromagnetic (FM) core and an antiferromagnetic (AFM) or ferrimagnetic (FiM) shell whereas inverted core-shell nanoparticles have an AFM core and an FM or FiM shell. The distinct magnetic phases in the core vs the shell regions interact via the exchange bias effect.[10–12] The inverted CSNs are particularly promising because their magnetic properties are more easily controlled, by having well-ordered AFM cores, resulting in magnetic structures having large coercivities, tunable blocking temperatures and other enhanced magnetic effects.[13,14]

The mechanism of the exchange bias effect is better understood in thin films than in bimagnetic CSNs. Ohldag et al.[15] showed that the source of the exchange bias field in NiO/Co, IrMn/Co, and PtMn/$Co_{90}Fe_{10}$ polycrystalline magnetic thin-film bilayers is due to uncompensated pinned spins at the interface between the AFM/FM layers. Kuch et al.[16] studied the exchange bias effect in well-ordered, epitaxially grown Co/FeMn-based multilayers and determined that the uncompensated pinned spins responsible for the exchange bias field were most prevalent in thin films having small islands with monatomic sized steps at the AFM/FM interface. In bimagnetic CSNs on the other hand, the size, shape, structural properties, inter-particle dipolar interactions, and the quality of the core-shell interface appear to play a role in governing their exchange bias and magnetic properties.[9] Experimental studies indicate that a low-quality, structurally disordered core-shell interface reduces the exchange bias in $Fe_2O_3$@$Mn_3O_4$[17] CSNs whereas a remarkably high exchange bias in $Fe_{3-\delta}O_4$@CoO[18] CSNs was in part attributed to a high quality core-shell interface. Weak room-temperature ferromagnetism in CoO@$Fe_3O_4$ octahedron-shaped nanocrystals was attributed to strained lattice correlations established at the high quality interfaces of the CSNs.[19] The role of defects and disorder (i.e., roughness) has also been addressed by computational means. Monte Carlo simulations were used to show that the presence of defects (vacancy or non-magnetic impurity) at the core-shell interface degrades

---

[a] Department of Physics, Astronomy & Materials Science, Missouri State University, Springfield, MO 65897.
[b] University of Arkansas Nano-Bio Materials Characterization Facility, University of Arkansas, Fayeteville, AR 72701, USA.
[§] Present Addresses: 420 Sand Creek Road, Albany, NY 12205.
† robertmayanovic@missouristate.edu.

Electronic Supplementary Information (ESI) available: [SEM, TEM, XPS, UV-Vis, DOS, p-DOS]. See DOI: 10.1039/x0xx00000x the exchange bias in FM@AMF CSNs.[20] In a separate study, it was shown from Monte Carlo simulations that spherical FM@AFM CSNs with smooth core-shell interfaces have higher exchange bias (EB) fields than ones having considerable interface roughness.[21] However other studies based on Monte Carlo simulations show that the magnitude of the exchange bias field is enhanced with greater interface roughness in FM@AFM core-shell nanoparticles.[22] More recently, several experimental studies have reported large EB fields for their bimagnetic CSNs and attribute this directly to closely lattice matched, sharp core-shell interfaces. The enhanced EB fields exhibited by FM@AFM Co@CoO CSNs were demonstrated to be due to a well-defined, relatively defect free interface and close lattice parameter matching, the latter being made possible by the $Cu_xO$ matrix surrounding the particles, between the core and shell.[23] Similarly, a very large EB field (8.6 KOe) was recently attributed to the high crystallinity, close lattice-matching and sharpness of the interface of AFM@FiM $Co_{0.3}Fe_{0.7}O@Co_{0.6}Fe_{2.4}O_4$ CSNs.[24] Thus, core-shell nanostructures having high quality, epitaxial core-shell interfaces are likely required to ensure proper switching behavior in magnetic devices via the exchange bias effect.[9] In addition, highly crystalline, well lattice matched and sharp interfaces are necessary in order to fully understand the complicated nature of the intrinsic exchange bias property of bimagnetic CSNs.

Room-temperature ferro- or ferrimagnetism, along with the exchange bias effect, is an essential element of bimagnetic CSNs for many future applications in magnetic devices (spintronics, spin valves, etc.), magnetic media storage, and biomedical therapy and diagnostics. Remarkably, despite vigorous research activity in the field, the number of reports of synthesis of bimagnetic CSNs having room-temperature FM/FiM properties is quite small.[25,26] One way of achieving room-temperature ferromagnetism/ferrimagnetism and sufficient exchange bias effect for therapeutic and device applications may be through development of novel bimagnetic CSNs that incorporate metastable phases. The metastable nanophases may provide unexpected and substantially enhanced magnetic properties that are not commonly observed in stable phases of the same materials. Additionally, $\alpha$-$Cr_2O_3$ has well known magnetoelectric properties that hold considerable promise for spintronic device applications. Voltage-induced switching of the exchange bias field via the magnetoelectric effect has been demonstrated in AFM/FM heterostructures.[27] Herein, we report on the synthesis and experimental characterization of $\alpha$-$Cr_2O_3$@$\alpha$-$Ni_{0.58}Cr_{1.42}O_{2.88}$ inverted CSNs, with a first-of-its-kind corundum-structured $Ni(II)_xCr_{2-x}O_{3-\delta}$ metastable compound constituting the shell of the CSNs. In addition, first principles calculations are made of $Ni_xCr_{2-x}O_3$, in order to better understand its magnetic and electronic properties. Our CSNs have a sharp, epitaxial interface between the AFM $\alpha$-$Cr_2O_3$ core and the $\alpha$-$Ni_{0.58}Cr_{1.42}O_{2.88}$ cluster-localized FM shell. As demonstrated by measurement and first principles modeling, the metastable $Ni(II)_xCr_{2-x}O_{3-\delta}$ nanophase of the shell enables room-temperature FM characteristics and exchange bias effects in the CSNs.

## Experimental Methods

We have developed a nature-inspired hydrothermal nanophase epitaxy (HNE) method for synthesis of highly ordered AFM core and a FM/FiM shell $Cr_2O_3$ – based CSNs.[28–30] By imitating mineral zonation that occurs naturally under hydrothermal conditions,[31] we are able to grow an epitaxial highly structurally ordered $\alpha$-$M_xCr_{2-x}O_{3-y}$ shell (M: Co, Fe, Ni, Mn) covering a $\alpha$-$Cr_2O_3$ nanocrystalline core to form $\alpha$-$Cr_2O_3$@$\alpha$-$M_xCr_{2-x}O_{3-y}$ inverted CSNs. Our methodology employs a two-step process. First, $Cr_2O_3$ nanoparticles (NPs) were synthesized following the procedure outlined in Farzaneh et al.[32] HPLC water and commercially available $Cr(NO_3)_3{\cdot}9H_2O$ (Sigma-Aldrich) were used for making a 0.2 M aqueous solution. The aqueous solution was subsequently mixed with an organic surfactant Triethanolamine (TEOA) in 1:2 molar ratio. The HPLC water was deoxygenated by passing dry nitrogen gas through it while maintaining the temperature at ~60 °C. The solution was magnetically stirred for 1 hour and irradiated in a microwave oven for 5 minutes. Subsequently, the solution was left on top of a magnet for ~6 hours whereupon a dark-green colored precipitate formed at the bottom of the beaker. The precipitate was separated from the solution and then dried in air. Next, the precipitate was calcined in air by heating at a rate of 10 °C/min to 575 °C, maintained at 575 °C for 2 hours, and finally cooled to room temperature at 10 °C/min. The sample turned into a green-colored fine powder after the calcination process. For shell overgrowth and CSN synthesis, a 0.05M solution (pH = 6.5) was first prepared from commercially available $NiCl_2$ by using deoxygenated HPLC water. Next 0.2997g of $Cr_2O_3$ nanoparticles (NPs) were added to the solution and sonicated for ~20 minutes and then loaded into a Teflon-insert autoclave. The nanoparticle/$NiCl_2$ solution was hydrothermally treated for ~13 hours at a temperature of 210 °C. Subsequently, the solution was transferred to a beaker and placed on top of a magnet for an extended period of time to allow for the NPs to be fully precipitated out of solution. After air drying, the nanoparticle sample was calcined at 500 °C for ~2 hours in forming gas: the heating and cooling rate were set at 10 °C/min.

The X-ray diffraction (XRD) analysis of the nanoparticles was made using the Bruker D8 Discover powder diffractometer having the characteristic x-ray radiation CuKα (λ = 1.54184 Å). The instrument was operated at 40 kV and 40 mA. A Göbel mirror was used to focus the incident x-ray beam. A 0.6 mm slit was used on the incident beam and a 0.6 mm slit on the detector side of the diffracted beam. An overall spectrum was obtained from averaging of three individual spectra. Rietveld refinement of the XRD patterns was accomplished using the TOPAS software.[33] Scanning electron microscopy (SEM) imaging and energy-dispersive x-ray (EDX) spectroscopic analyses of the nanoparticles were made using an FEI Quanta

200 instrument operating at 30.0 kV. The sample was dispersed on conductive carbon tape and EDX analysis was performed on the sample using a field emission gun (FEG). Transmission electron microscopy (TEM) samples were prepared by dispersing the $\alpha$-$Cr_2O_3$@$\alpha$-$Ni_{0.58}Cr_{1.42}O_{2.88}$ CSNs in hexane followed by submerging the lacey carbon grid in the hexane-nanoparticle solution and subsequently drying the sample. TEM analysis was performed at the University of Arkansas Nano-Bio Materials Characterization Facility using a Titan 80-300 with the field emission gun operated at 300 keV. The simulated selected area electron diffraction (SAED) patterns were generated from the TEM images using the fast Fourier transform (FFT) algorithm within imageJ.[34] The x-ray photoelectron spectroscopy (XPS) analysis was made using an Al K-alpha source with a characteristic energy of 1486.6 eV. The Ag $3d_{5/2}$ peak (FWHM = 0.36 eV) was used for calibration of the source and analyzer. A Thermo Scientific Alpha 110 hemispherical analyzer with a pass energy of 25 eV was utilized for collection of the XPS spectra. The CasaXPS 2.3.16 software was used for analysis and peak fitting of the XPS spectra**.** Shirley and Tougaard background types were used for XPS peak fitting within the CasaXPS software package. The Gaussian-Lorentzian product GL(30) functions were used in the fitting of the peak line shapes. The magnetic measurements were made using a SQUID magnetometer from Quantum Design (MPMS/XL) used from a temperature range of 5K-330K and in a field of ± 5 kOe. A quantity of 40 mg of sample was placed in a gelatin capsule, which was positioned within the SQUID and inside the low temperature vessel of the instrument for the magnetic measurements. The field cooling for the magnetic hysteresis curve measurements was accomplished starting from 330 K to below the Néel temperature of the sample in a field of 20,000 Oe. In the case of field cooled (FC) magnetization measurements vs temperature, the sample was cooled in a field of 500 Oe starting from 330 K. Additional experimental procedures are provided in the Electronic Supplementary Information.

## Calculation Methods

The first principles calculations were made using the Local Spin Density approximation method[35] (LSDA) implemented in Quantum Espresso.[36] A rhombohedral primitive unit cell[37] with a space group $R\bar{3}cH$ (ICSD 173470) was used in the initial self-consistent field calculation of $Cr_2O_3$. To find the equilibrium ground state and the corresponding magnetic configuration of $\alpha$-$Cr_2O_3$, the FM, AFM and nonmagnetic (NM) systems were considered. The +-+- alignment along the z-axis AFM spin configuration (out of several possibilities, such as ++--, +--+, etc.) calculation converged to the lowest energy. The Monkhorst-Pack scheme[38] based on the 4x4x4 k-point grid was employed for Brillouin-zone integral calculations. The plane wave and augmentation charge cutoff energies were set at 30 and 300 Ry, respectively: Energy convergence was obtained at a value of 0.097961 μeV, as a result of fixing the atomic energy convergence to $1\times10^{-8}$ eV. The density of states (DOS) were obtained for the relaxed structure by using the tetrahedron method with an 8x8x8 k-point grid mesh. For spin polarization calculations, LSDA+U, where U is the Coulomb repulsion parameter, and local exchange interaction (J) were used in order to obtain results more consistent with experimentally derived values. The values of the U and J were adopted from a previous first principles calculation study of chromia.[39] For calculations of Ni-substituted $\alpha$-$Cr_2O_3$, either $\alpha$-$NiCr_3O_6$ in the 1x1x1 cell or $\alpha$-$Ni_2Cr_6O_{12}$ in the 1x1x2 supercell, the U and J values were adopted from Cococcioni et. el.[40] and Perdew-Zunger[41], where exchange-correlational, non-relativistic norm conserving pseudopotentials were used for all the atoms. Calculations of the 1x1x1 cell and 1x1x2 supercell were made in the charged (i.e., Ni(II)) state, where a homogeneous background charge was incorporated in the charged state calculations prior to optimization of the structure. The $\alpha$-$Ni_xCr_{2-x}O_3$ structures were relaxed for energy minimization and the relaxed structural parameters were used in subsequent calculations. The relaxed structural parameters were obtained until all the forces were less than $1\times10^{-3}$ eV/a.u. The electron localization function[42,43] images were generated by using the visualization software Vesta.[44]

## Results and Discussion

SEM and TEM images shown in Figs. S1 and S2 of the Electronic Supplementary Information (ESI), respectively, indicate that the majority of the nanoparticles (NPs) manifest in quasi-spherical or nanocrystalline morphology with an average particle size of ~57(3) nm. Fig. 1 shows the results from high resolution TEM (HRTEM) imagery and structural analysis of our CSNs. As shown in Fig. 1a), well-defined crystal planes and core-shell architecture are clearly visible in the HRTEM image of a select CSN. The well-defined fast Fourier transforms (FFTs) shown in Figs. 1b) and c) indicate the high crystallinity of both the core and shell regions, respectively. Fig. 1g) shows a close-up view of a portion of the core-shell interface. A slight discontinuity and change in contrast are observed (Figs. 1a) and g)) approximately 5 nm from the surface, delineating the shell from the core region of the CSN. Although well defined, some structural defects such as dislocations, vacancies and stacking faults are observed in the core-shell interface. Line-profile TEM energy dispersive spectroscopy (TEM- EDS) shown in Fig. 1f) clearly shows that whereas Cr and O are uniformly distributed throughout, Ni is predominantly distributed in the shell region of the CSNs. The nanoparticle size of 57(2) determined using analysis of the XRD data shown in Fig. 2, using either the Scherrer equation or Rietveld refinement (integral breadth method), is in excellent agreement with the TEM and SEM analyses. Fig. 2a) shows the XRD data of the Ni-chromia CSNs. The corundum structure having the space group $R\bar{3}cH$ (ICSD#173470) was used for both the core and shell contributions. The Rietveld refinement of the core-shell structure was accomplished with a weight profile R-factor ($R_{wp}$) value of 2.44; refinement of the same experimental data without considering a core-shell structure to the nanoparticles resulted in a significantly poorer fit with an $R_{wp}$ value of 3.22 (this fit is shown in the inset of the Fig. 2 a)).

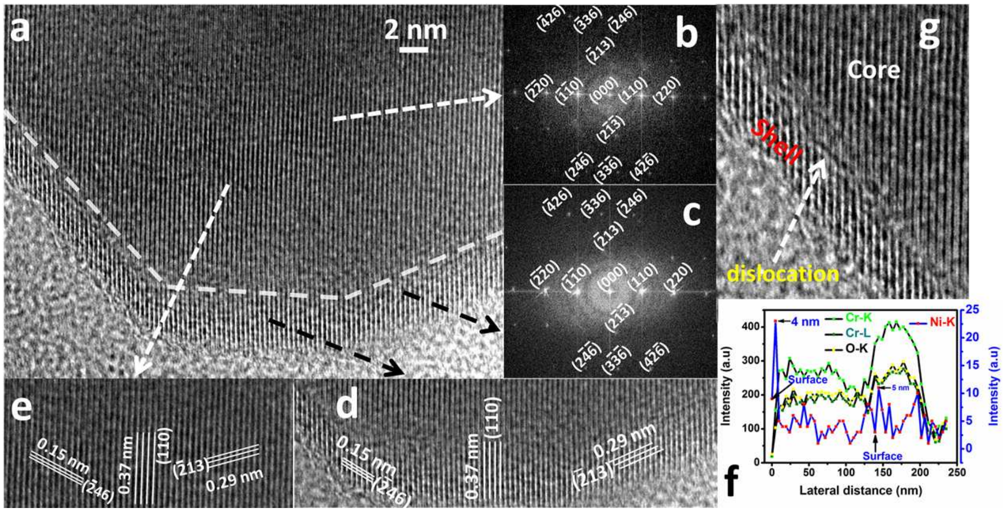

Fig. 1(a). An HRTEM image showing the core-shell structure of a α-$Cr_2O_3$@α-$Ni_{0.58}Cr_{1.42}O_{2.88}$ nanoparticle; (b) FFT of the core and the (c) FFT of the shell of the CSN; several atomic planes and corresponding d-spacings between the planes in the (d) shell the same atomic planes (as in shell) and corresponding d-spacings between the planes in the (e) core; (f) TEM-EDX elemental line profile of two side-by-side nanoparticles; (g) a close-up view showing a few dislocations that are evident at the core-shell interface.

The structural results obtained from the Rietveld refinement are provided in Table S1 of the ESI. The Rietveld refinement of the XRD data along with the HRTEM analyses are fully consistent with the corundum $R\bar{3}c$ structure being persistent throughout the core and shell of the CSNs; this combined with the HRTEM image analysis indicates continuity of the crystal planes across the interface between the two regions. Our XRD and HRTEM results indicate that Ni is incorporated substitutionally for Cr in the CSNs. Figs. 2b), c) and d) show the fitting analysis of the high resolution XPS Cr2$p_{3/2}$, O1s, Ni2$p_{3/2}$ peaks, respectively. The O1s peak is composed of 3 deconvoluted peaks, at 530.34 eV and 528.9 eV due to the Cr-O and Ni-O bonding, respectively, and one at 530.97 eV corresponding to the Cr-OH and Ni-OH bonding in the CSNs. The overall Cr2$p_{3/2}$ peak has two contributions: The multiplet splitting phenomena gives rise to a broadened peak, where the peak positions represent Cr-O bonding consistent with the +3-oxidation state of Cr; the secondary peak at 577.04 eV is due to Cr-OH bonding. Fitting of the high resolution XPS Ni 2$p_{3/2}$ peak at 853.42 eV indicates Ni-O bonding with Ni in the +2-oxidation state in the CSNs; a Ni-OH bonding component is evidenced by the peak at 854.95 eV. The details of the high-resolution XPS analyses are provided in Table S2 in the ESI. Elemental analyses made from XPS (see Table S3 and further details provided in the ESI) and from the Rietveld refinement of the XRD data using methods outlined in our previous reports,[28,30] indicate that the nanophase compound of the shell has an approximate formula given by $Ni_{0.58}Cr_{1.42}O_{2.88}$. A small sub-stoichiometry with respect to oxygen content is expected, in order to maintain charge balance upon substitution of $Ni^{2+}$ for the $Cr^{3+}$ ion in the shell region of the CSNs. The authors are aware of only one study reporting on the preparation of Ni(II)-doped (to ~ 4 mol%) $Cr_2O_3$ NPs.[45] This study reports that attempts at synthesis of Ni(II)-doped $Cr_2O_3$ NPs having greater Ni concentrations resulted in precipitation of a $NiCr_2O_4$ spinel NP phase, consistent with solid solution studies of the bulk NiO-$Cr_2O_3$ system.[46] Thus, our α-$Cr_2O_3$@α-

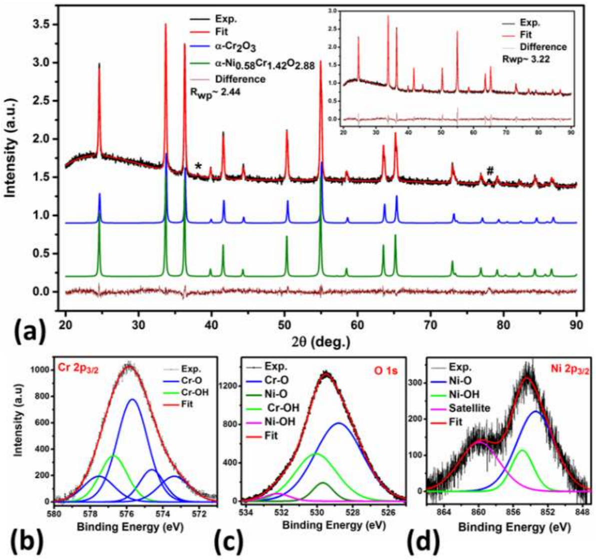

Fig. 2(a). XRD data (black line) measured from the α-$Cr_2O_3$@α-$Ni_{0.58}Cr_{1.42}O_{2.88}$ CSNs at ambient conditions and the Rietveld refinement of the data (red line). The individual contributions from the α-$Cr_2O_3$ core (blue line) and the α-$Ni_{0.58}Cr_{1.42}O_{2.88}$ shell (green line) are shown in the figure. The inset shows the Rietveld refinement fit using only one structure without considering distinct core and shell contributions. Very minor amounts of a NiO phase (marked with *) and an unknown impurity phase (marked #) are present in the sample. b) High resolution XPS data measured from the α-$Cr_2O_3$@α-$Ni_{0.58}Cr_{1.42}O_{2.88}$ CSNs (black line), the overall fit to the data (red line) and the contributions to each peak (lines in various colours) for the (b) Cr 2$p_{3/2}$, (c) O 1s, and (d) Ni 2$p_{3/2}$ peaks.

$Ni_{0.58}Cr_{1.42}O_{2.88}$ CSNs contain a shell composed of a metastable, corundum-structured nickel-chromia nanophase compound that has been synthesized for the first time. The metastable nickel-chromia nanophase is made possible by the epitaxial growth of the shell of the CSNs.

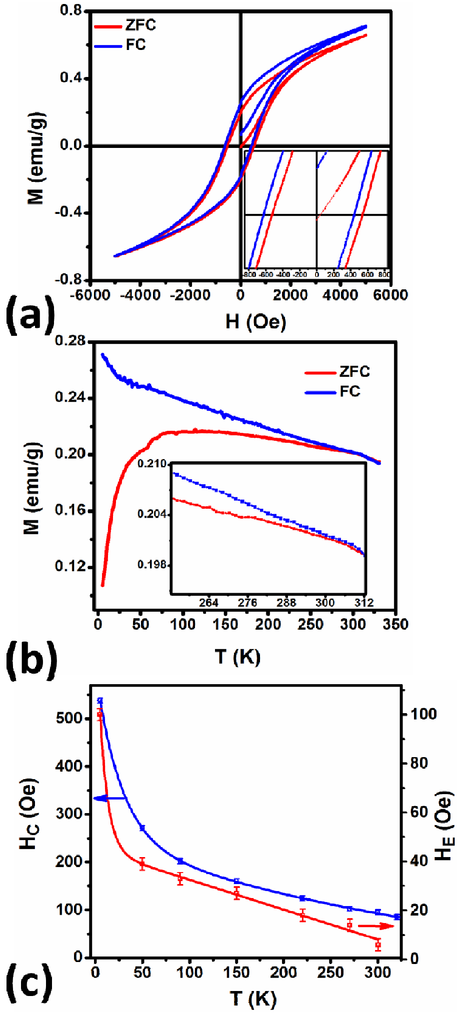

Fig. 3(a). Hysteresis curves measured from α-$Cr_2O_3$@α-$Ni_{0.58}Cr_{1.42}O_{2.88}$ CSNs at 5 K in the zero-field cooled (ZFC) and field cooled (FC) condition at 20 kOe. The inset shows the shift between the FC and ZFC hysteresis curves due to the exchange bias effect near zero applied field. (b) The ZFC and FC magnetization as a function of temperature measured from the CSNs at 500 Oe. The inset shows the data in the vicinity of the bifurcation temperature (311 K). (c) The temperature dependence of the coercivity ($H_C$) and the exchange bias ($H_E$) fields, as determined from the hysteresis curves measured from the CSNs at different temperatures.

Fig. 3a) shows zero field cooled (ZFC) and field cooled (FC) magnetic hysteresis measurements made at 5 K and in the -5 to +5 KOe applied magnetic field (**H**) range. The FC magnetization (M) vs applied magnetic field hysteresis loop is shifted vertically along the magnetization axis and in the negative field direction with respect to the ZFC loop, due to the exchange bias effect evident in the CSNs. This is consistent with the magnetic hysteresis loop behavior exhibited by inverted CSNs. The value of the exchange bias field, as defined using $H_E = |(H^+ + H^-)|/2$,[47–49] where $H^+$ and $H^-$ are the coercive field FC values for ascending and descending hysteresis curves, respectively, is ~100 Oe at 5K. This is consistent with an interaction between a FM shell and an AFM core of the CSNs.[14] Indeed, magnetic measurements of our α-$Cr_2O_3$ NPs prior to synthesis of CSNs show that these exhibit solely AFM properties (see Fig. S5 in the ESI for further details). Fig. 3b) shows the magnetization with respect to temperature measured from 5 to 330 K in the ZFC and FC condition. The Néel temperature ($T_N$) of the AFM α-$Cr_2O_3$ core of our nanoparticles, as determined from the kink in that region of the ZFC curve, is found to be 308 K (see also inverse susceptibility data shown in Fig. S6 of the ESI). An additional kink observed near 27 K may be due to a spin order-disorder transition. This value is slightly higher than the reported value of 302 K for $Cr_2O_3$ nanoparticles (50-70 nm dia.)[50] and same as the value reported for bulk $Cr_2O_3$.[50] The relatively large value of the coercivity $H_C = |(H^+ - H^-)|/2 = 533$ Oe at 5K is consistent for both the ZFC and FC hysteresis loops. The measured $H_C$ values were found to be essentially the same for both the ZFC and FC hysteresis curves throughout the measured temperature range for our CSNs. This is contrasted with the results for FeO-$Fe_3O_4$[51] and MnO-$Mn_3O_4$[52] CSNs, showing that the $H_C$ values are significantly enhanced for the FC curves, for which these results were attributed to their strong uniaxial anisotropy. Thus, our results are consistent with a relatively weak uniaxial anisotropy in our CSNs. The ZFC and FC M vs T curves start to deviate from one another at a bifurcation temperature of 311 K. The blocking temperature $T_B$ of the CSNs is 102 K, as identified by the maximum in the ZFC magnetization curve. This blocking temperature coincides with superparamagnetic behavior and is due to the FM property (as will be established below) of the $Ni_{0.58}Cr_{1.42}O_{2.88}$ shell of the CSNs. Because this is the first study to report on a novel metastable $Ni_xCr_{2-x}O_{3-\delta}$ phase, there are no previous data to compare on the superparamagnetic properties of its nanostructures. Nevertheless, our value is quite reasonable when compared to $T_B$ values reported for CoO-core-based CSNs having $Co_xFe_{3-x}O_4$ FiM shells.[24] This indicates that the effective anisotropy constant K ($T_B \propto KV$, where V is the shell volume) of the FM shell is sufficiently large to result in the observed superparamagnetic properties for our CSNs.

Fig. 3c) shows the dependence of $H_C$ and $H_E$ on temperature in the 5 to 330 K range. Both the $H_C$ and $H_E$ vs temperature data were fitted using a double-exponential decay function. The first significant feature shown in Fig. 3c) is the persistence of the coercivity of the CSNs above room temperature, i.e., $H_C$ = 82(3) Oe at 330 K. This indicates that the FM properties persist beyond room temperature and that the Curie temperature ($T_C$) of the CSNs lies beyond 330 K. The second significant feature shown in the same figure is the persistence of a weak exchange bias field at room temperature (see Fig. S7 in the ESI for hysteresis curve measurements made at various temperatures). Clearly, the temperature-dependent behavior of the core, specifically the transition from the AFM to the paramagnetic state at $T_N$, strongly affects the exchange bias effect in the CSNs. Although not shown on Fig. 3(c), our measurements show that $H_E$ is 0 Oe at 330 K. Thus, the transition from the AFM to the paramagnetic state of the $Cr_2O_3$ core causes a de-pinning of any remaining pinned uncompensated spins at the core-shell interface leading to a complete quenching of the exchange bias effect in our CSNs. Although obviously highly desirable for practical applications, reports of nanoparticle-based materials having both room-temperature FM/FiM and exchange bias properties are extremely rare: To our knowledge, there is only one other report of this nature for Co@CoO core-shell nanocrystals.[26] Gonzalez et al.[23] have demonstrated that the blocking of the exchange bias field of their Co@CoO CSNs, which is attributed to the average anisotropy of the CoO component, is extended farthest in temperature for shells having the highest crystallinity. It is plausible that the persistence of $H_E$ to near room temperature is similarly attributable to the high crystallinity of the $Ni_xCr_{2-x}O_{3-\delta}$ shell of our CSNs. The inverted nature of our CSNs should allow for a high degree of tunability of their magnetic properties (i.e., $T_B$, $H_E$, $H_C$, and $T_C$) through adjustment of core vs shell size, shell composition, and morphology. Such tunable properties are important for practical applications, such as in spintronics, spin valve, and magnetic random-access memory, where switching between hard (FM) and soft (AFM) characteristics is critical for the operation of the device.

We have made DFT-based calculations in order to determine the magnetic and electronic properties of the metastable $\alpha$-$Ni_xCr_{2-x}O_3$ phase contained in the shell of our CSNs. In Fig. 4 we show the electronic DOS and partial density of states (pDOS; of the cations) calculated for chromia ($\alpha$-$Cr_2O_3$) and Ni(II)-substituted chromia ($\alpha$-Ni(II)$Cr_3O_6$). The Ni substitution was made in the Cr3 site in the1x1x1 rhombohedral primitive unit cell (see Fig. 5). Substitution with Ni for one Cr in the cell is roughly consistent with the Ni content in the Ni-chromia nanophase compound of the shell in the CSNs. The band gap energy value for $\alpha$-Ni(II)$Cr_3O_6$ was determined from our calculations to be 2.55 eV, as defined by the gap between Cr-Ni majority-spin 3d $t_{2g}$ sub-band contribution to the overall valence band (VB) and O 2p levels in the conduction band (CB) (see Fig. 4 and Fig. S9 in the ESI ).[53] UV-Vis absorption measurements yield an optical band gap value of 2.5(1) eV for our $\alpha$-$Cr_2O_3$@$\alpha$-Ni(II)$_{0.58}Cr_{1.42}O_{2.88}$ CSNs (see Fig. S8 in the ESI), which is in excellent agreement with our calculations. Thus, we observe a band gap energy narrowing for $\alpha$-Ni(II)$Cr_3O_6$ in comparison to either our calculated value of 3.15 eV or with the experimentally determined values ranging from 3.2 to 3.4 eV for $\alpha$-$Cr_2O_3$.[54–56] Despite the narrowing, the energy band gap is sufficiently large so that our CSNs are adequately insulating for switchable magnetic device applications. As seen in Fig. 4d), there is a significant impurity-like energy level 3d $e_g$ contribution predominantly from Ni3, with minor contributions from Cr1, Cr2 and Cr4, to a DOS projection in the middle region of the band gap. The impurity energy levels (IELs), which stem from hybridization of predominantly delocalized Ni 3d states with O 2p states, can enable acceptor- and donor-like optical transitions.

As shown in Figs. 4a) and b), our self-consistent field calculations yield exactly opposing majority (spin up) and minority (spin down) spin state DOS contributions with a magnetic moment value of 3.11 $\mu_B$ for each Cr, which is slightly higher than the experimental value of 2.76 $\mu_B$,[57] in the AFM $\alpha$-$Cr_2O_3$. Conversely, as shown in Figs. 4c) and d), our calculations show that Ni substitution creates an imbalance in the 3d contribution to the spin state DOS, yielding an overall net magnetic moment of 2.96 $\mu_B$ in $\alpha$-Ni(II)$Cr_3O_6$. Furthermore, the spin polarization calculations show that the Ni spin is flipped in orientation with respect to that of the original Cr atom and has a magnetic moment value of +0.12 $\mu_B$ (see Table S4 in the ESI). The marked reduction in the magnitude of the magnetic moment of Ni, in comparison to previously determined theoretical values of 1.64 $\mu_B$ in metallic nickel particles[58] and 1.9 $\mu_B$ in $Mn_xNi_{1-x}O$,[59] is attributed to strong hybridization (within the VB and inter band gap states) of the Ni 3d levels and O 2p levels of the surrounding oxygen atoms. Formally, in the high spin state (in octahedral coordination), $Ni^{2+}$ has 6 paired electrons in the 3d $t_{2g}$ levels and 2 unpaired electrons in the 3d $e_g$ levels. In the case of $\alpha$-Ni(II)$Cr_3O_6$, the electrons in the $Ni^{2+}$ 3d $e_g$ levels near the top of the VB are paired, as evidenced in the near cancelation of the spin-up and spin-down Ni $e_g$-contributions to the pDOS (see Fig. 4 and Fig. S10 in the ESI). The strong hybridization of the VB Ni 3d levels and O 2p levels is consistent with our Bader charge analysis[60,61] of $\alpha$-$NiCr_3O_6$ (relative to its full ionic state) when compared to that of $\alpha$-$Cr_2O_3$. Upon substitution of Ni(II) we find considerably reduced localization of charge on Ni(+0.55e; e ≈ 1.6 x $10^{-19}$ C) than on Cr sites (~+2.5e) and a reduction in charge on O sites by 0.08 to 0.27e compared to the values in $\alpha$-$Cr_2O_3$ (see Table S5 in the ESI). The reduced ionic charge of

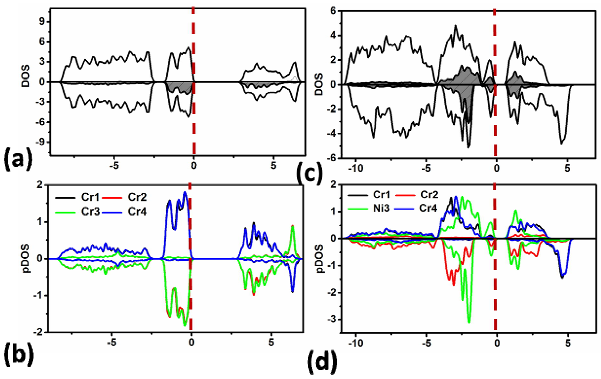

Fig. 4(a). The DOS (shaded portions show contributions from Cr3 3d orbitals) and (b) the partial density of states (pDOS) for Cr 3d orbitals as determined from DFT-based calculations for chromia, and (c) the DOS of Ni(II)-substituted chromia (shaded portions show contributions from Ni3 3d orbitals) and d) the pDOS for Ni and Cr 3d orbitals. The Fermi level is indicated by the vertical dashed line.

the O atoms indicates charge transfer from the O 2p to the shared cation-anion orbitals. Additionally, we have used electron localization function (ELF) analysis,[42,43] which provides a measure of electron redistribution surrounding the core or nucleus of the individual atoms. Figs. 5a) and b) show the ELF plots for $\alpha$-$Cr_2O_3$ and $\alpha$-Ni(II)$Cr_3O_6$ projected along the $(\overline{12}35)$ plane, respectively. This plane was chosen to provide an optimal projection of the cation-oxygen-cation ~90-degree bonding arrangements, in the hexagonal unit cell shown in Fig. 5d). The ELF plots show that the electron densities of the Cr and O atoms have nominal overlap and commensurate (partial) Cr – O covalent bonding in $\alpha$-$Cr_2O_3$ but significantly greater Ni – O (e.g., O1 and O3) electron density overlap and more substantial Ni – O covalent bonding in $\alpha$-Ni(II)$Cr_3O_6$.

As shown in Fig. 5d), the equilibrium spin configuration that emerges from our calculations for $\alpha$-Ni(II)$Cr_3O_6$ is one in which the Ni and Cr spins are aligned parallel to one another within the (0001) buckled honeycomb (BH) planes, i.e., the Ni3 spin flips with respect to the original orientation of the Cr3 spin in chromia. Our calculations show that the overall magnetic moment results predominantly from the majority spin (3d $t_{2g}$) state contribution due to Cr1, whereas the moments due to Cr2 and Cr4 cancel one another: The small moment on the Ni3 site adds to that of the one on the Cr1 site. The increased covalency of the Ni – O bond compared to that of the Cr – O bond is consistent with the reduced magnetic moment on the substitutional Ni(II) ion in $\alpha$-Ni(II)$Cr_3O_6$. Thus, our calculations correctly predict the FM property of our CSNs. Interestingly, our calculations of $\alpha$-Ni(III)$_{0.5}$Cr$_{1.5}$O$_3$ (i.e., $Ni^{3+}$ substitution), that will be published in the near future, predict a weaker overall magnetization effect but better suitability for spintronic device applications because of its half-metallic characteristics.

In order to test different Ni site occupancies and influence of varying proximity of Ni(II) ions on the magnetic properties of a Ni(II)-chromia compound, first principles calculations have been carried out on a 20 atom 1x1x2 supercell containing $\alpha$-Ni(II)$_2$Cr$_6$O$_{12}$ (i.e. a doubling of the primitive unit cell; see Fig. S11 in the ESI). Several variations of starting positions and initial spin orientations were attempted, in order to determine the equilibrium spin structure, energy and overall magnetic moment of $\alpha$-$Ni_2Cr_6O_{12}$. One of the most interesting cases occurs for Ni occupation within the (1114) planes but in alternate BH planes; another case is for "farthest-removed" Ni occupation but within the same BH plane. The equilibrium spin configuration confirms parallel Ni-Cr spin coupling in the BH plane and a net magnetization moment of ~5.9 $\mu_B$ in the 1x1x2 cell (See Table S6, Case-5, in the ESI). The model that emerges from the calculations that test the more random Ni substitution in Ni(II)-chromia is one of FM clusters centered upon Ni sites embedded within an AFM matrix: In some cases, such as close proximity of Ni's in the same BH plan, the moments cancel whereas in other cases, such as Ni occupation in complementary site occupation in adjoining BH planes, the moments add to give an overall FM value. Thus, our calculations demonstrate that $Ni^{2+}$ substitution for $Cr^{3+}$ results in a localized FM spin configuration within a corundum structured $\alpha$-Ni$_{0.58}$Cr$_{1.42}$O$_{2.88}$ shell of our CSNs. Both the 1x1x2 supercell and the 1x1x1 primitive cell calculations show that the cation 3d states, particularly those stemming from Ni, dominate over the O 2p states near the top of the VB and at the bottom of the CB in the DOS of Ni(II)-chromia. Thus, based on our calculations, the Ni(II)-chromia compound is a Mott-Hubbard insulator.

As shown above, our calculations demonstrate that localized FM ordering in our CSNs is only predicated upon substitution of Ni(II) for Cr(III) in the corundum structure and the resultant electronic density of states. Nevertheless, it needs to be borne in mind that the DFT-based calculations do not take into account potentially significant nano-scale effects of our CSNs. These include surface and/or interface spin disorder[12] (e.g., spin glass layers) and spin anisotropy effects present on nanostructures. Our DFT-based calculations also do not take into account the finite size effects of core-shell nanoparticles. A more effective method to account for the finite size of CSNs, including for the EB effect, is by use of $Cr_2O_3$/$Ni_xCr_{2-x}O_3$ slab DFT-based calculations, where the top $Ni_xCr_{2-x}O_3$ layer of the slab is terminated by vacuum. These calculations are beyond the scope of the present work but are presently underway and

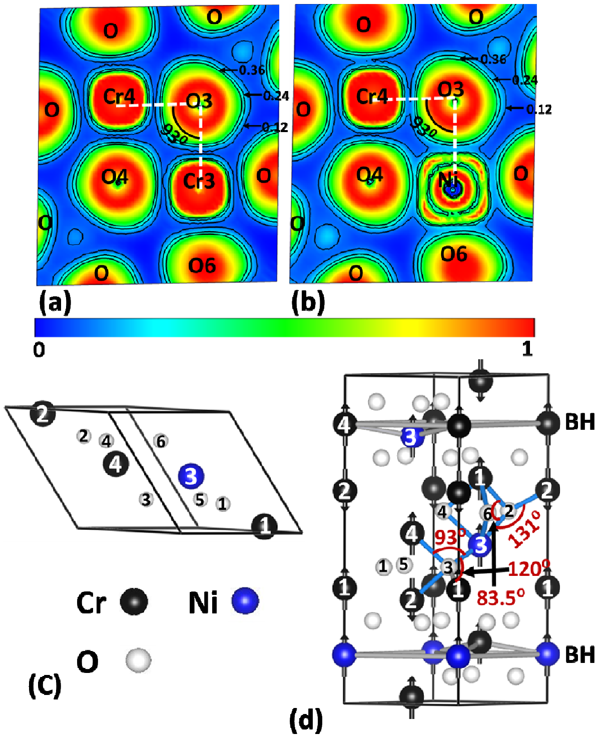

Fig. 5. ELF contour diagram plots projected over the $(\overline{12}35)$ plane in the hexagonal unit cell of (a) $\alpha$-$Cr_2O_3$ and (b) $\alpha$-Ni(II)$Cr_3O_6$ : the 0.12, 0.24, and 0.36 isosurface contours are shown. (c) The 1x1x1 primitive rhombohedral unit cell used in the ab initio calculations for $\alpha$-$Cr_2O_3$ and for $\alpha$-Ni(II)$Cr_3O_6$; the atomic positions used in the calculations are labeled as shown. (d) A hexagonal unit cell showing Ni substitution for Cr and the resultant equilibrium FM ordering within the buckled honeycomb (BH) (0001) planes.

will be reported on in the future. In addition, the F-center exchange (FCE) coupling,[62] which occurs by interaction of $Ni^{2+}$-$V_O$-$Ni^{2+}$, where $V_O$ is the oxygen vacancy, may potentially play a role in establishing the FM properties of our CSNs. Our recent DFT-based calculations show that an oxygen vacancy has a significant effect on the redistribution of the electronic charge and consequently on the localized spin configuration of the cations in its immediate vicinity in Fe(II)-chromia.[63] However, further calculations are required in order to fully explore potential FCE coupling in $\alpha$-$Ni_xCr_{2-x}O_{3-y}$ and related phases for a range of x values. All of the effects described above have been invoked as potential mechanisms that result in FM/FiM properties and thereby play a direct role in exchange coupling of inverted CSNs.

After subtracting the AFM $\alpha$-$Cr_2O_3$ contribution (see ref. 63), the FC saturation magnetization ($M_s$) obtained from the M(H) hysteresis data measured at 5 K is 0.53 emu/g for our CSNs. Using this $M_s$ value, we estimate the average net magnetic moment per atomic formula unit (afu) to be 0.28 $\mu_B$/afu. Our DFT calculations show that for equivalent Ni content, the magnetic moment is 1.88 $\mu_B$/afu for isolated Ni site occupation (from the 1x1x1 calculation) whereas the average magnetic moment is 0.723 $\mu_B$/afu for proximal FM Ni-Ni pairing (from the results shown for cases 5 and 6 in Table S6 of the ESI). Some of the contributing factors for the discrepancy between the calculated and the experimental magnetic moment per afu values are canted spins occurring at the surface and interface regions, defects (e.g., cation vacancies, misfit dislocations, etc.), and proximal AFM Ni-Ni pairing (cases 1 – 4 in Table S6 of the ESI) occurring in the shell regions of the CSNs. In addition, it is likely that magnetic domains are formed within the CSNs owing to the size of the shell, leading to further reduction in their overall magnetization at low temperatures.

The competition between the interface spin-spin coupling strength vs the AFM anisotropy of the core has a direct bearing on the magnetic properties exhibited by nanostructured materials.[12] If the interface spin-spin coupling strength dominates, a strong AFM-FM or AFM-FiM exchange coupling ensues causing in turn a significant enhancement of the effective anisotropy and results in an increase of $H_C$. If, on the other hand, the AFM anisotropy dominates, the torque required for reversal of the magnetization increases resulting in enhanced $H_E$ values. Our estimates for the AFM anisotropy energy (given by $25k_BT_B$; $k_B$ is the Boltzmann constant) and exchange AFM-FM energy (given by $H_EVM_s$) are 3.5 x $10^{-13}$ erg and 1.2 x $10^{-15}$ erg, respectively.[12] Thus, the AFM anisotropy is dominant in our CSNs. This is consistent with our results showing that $T_B$ occurs below $T_N$. Superparamagnetic blocking below $T_N$ has been attributed previously to be due to finite size effects of the AFM portion of bimagnetic CSNs (see reference 12 and references therein). Thus, we infer that the AFM anisotropy of the $Cr_2O_3$ core is insufficient in pinning all of the uncompensated spins at the core-shell interface of our CSNs due to thermal fluctuations that occur beyond the blocking temperature $T_B$.

Furthermore, estimates of $H_E$ and $H_C$ based on the results from our DFT calculations, where we assume a reasonable statistical distribution of isolated and proximal Ni-cation substitution and contributions from pinned uncompensated spins at the core-shell interface to $H_E$, yields values of approximately 54 and 461 Oe, respectively. Although the value for $H_C$ is fairly reasonable, the value for $H_E$ calculated from theory is clearly considerably lower than the experimental value measured at 5K, suggesting that additional effects may contribute to the EB effect. It is plausible that defects in spin structure, such as spin canting or spin disorder in the core-shell interface region, and finite size effects provide additional mechanisms that enhance the magnetic properties of the CSNs, particularly the EB effect. As we have discussed previously for our $\alpha$-$Cr_2O_3$@$\alpha$-$Fe_xCr_{2-x}O_{3-\delta}$ CSNs,[63] the spin disorder in the core-shell interface region may provide additional pinned uncompensated spins and give rise to a perpendicularly-coupled anisotropy (at the core-shell interface) that enhances the magnetic properties of our Ni-chromia based CSNs. Although direct evidence for such an effect in CSNs has not been reported so far to our knowledge, Lottini et al.[24] have recently alluded to a perpendicular inter-coupling to explain the results from magnetic measurements of their $Co_{0.3}Fe_{0.7}O$@$Co_{0.6}Fe_{2.4}O_4$ CSNs. Low-temperature neutron diffraction measurements may help to resolve some of the details of the spin structure of our CSNs.

Due to its non-equilibrium nature, the HNE method enables growth of a shell containing a first-of-its-kind metastable Ni(II)-chromia nanophase compound over a chromia core resulting in epitaxial CSNs. Whereas synthesis of bimagnetic CSNs from structurally incompatible materials (for epitaxy) typically results in low quality core-shell interfaces, our method enables growth of shells of metastable nanophases on nanoparticle cores having high quality interfaces and epitaxially grown shells.[28–30] In agreement with the recent reports of substantial EB effects in other core-shell nanostructures,[23,24] we infer that the epitaxial nature and relatively defect-free core-shell interfaces are responsible for the persistence of the exchange bias effect in our $\alpha$-$Cr_2O_3$@$\alpha$-$Ni_xCr_{2-x}O_{3-\delta}$ CSNs to room temperatures. The high-quality interfaces make possible systematic studies of how the shape, size, and intra-particle dipolar interactions (e.g., by NP isolation in a suitable matrix) affect the EB and magnetic properties of our chromia-based CSNs. Finally, we note that due to the incorporation of $Ni^{2+}$ ions and the resulting oxygen vacancy formation on the surface, our $\alpha$-$Cr_2O_3$@$\alpha$-$Ni_xCr_{2-x}O_{3-\delta}$ CSNs should be suitable for tailored, multifunctional applications (e.g., magnetic, photocatalysis, heterogeneous catalysis, gas sensing, etc.). In particular, due to the energy band gap narrowing, IEL formation and cation d-level contribution to the bottom of the conduction band, our CSNs may have suitable semiconductor properties that are favorable for catalysis involving oxidation reactions. Further studies are required in order to fully test this hypothesis.

## Conclusions

We have successfully synthesized novel $\alpha$-$Cr_2O_3$@$\alpha$-$Ni_{0.58}Cr_{1.42}O_{2.88}$ inverted core-shell nanoparticles using our hydrothermal nanophase epitaxy (HNE) method. HR-TEM and

XPS analysis of the core-shell nanoparticles indicates a $\alpha$-$Cr_2O_3$ core with an average size of 57(3) nm and ~ 5 nm thick $\alpha$-$Ni_{0.58}Cr_{1.42}O_{2.88}$ shell; the XPS shows that Ni is in the +2-oxidation state within the shell. HR-TEM and XRD analyses indicate that the core-to-shell corundum structure of the nanoparticle is continuous (i.e., epitaxial registry) and a relatively sharp, defect-free core-shell interface. The SQUID magnetometry measurements confirm the inverted nature of our core-shell nanoparticles having enhanced magnetic properties (e.g., large coercivity of 533 Oe and an exchange bias of 96 Oe at 5 K). Our magnetic measurements show that the FM ordering and a weak exchange bias field persist to room temperatures in our CSNs. Our first principles DFT-based calculations confirm the equilibrium localized FM spin configuration of the shell. Furthermore, our calculations show that the cation-oxygen bonding environment in the immediate vicinity of the substituted Ni has increased covalency, due to the strong Ni 3d – O 2p hybridization in the upper valence band and band gap regions of the electronic energy band structure. The calculations show that Ni(II)-chromia is a Mott-Hubbard insulator. The structural selectivity exhibited by our HNE method should be useful for synthesis of target-specific, metastable nanomaterials having enhanced properties (e.g., superconducting, electronic, optical, etc. properties).

## Conflicts of interest

There are no conflicts to declare.

## Acknowledgements

S.D. and R.A.M. acknowledge partial support from EFree, an Energy Frontier Research Center funded by the US Department of Energy, Office of Science, Office of Basic Energy Sciences under Award Number DE-SC0001057. We thank Alexander Jankovic of the JVIC center at MSU for making the XPS measurements on our samples. We also thank Ariful Haque for help with the magnetic measurements. This work used the Extreme Science and Engineering Discovery Environment (XSEDE), which is supported by National Science Foundation grant number ACI-1053575. We thank the reviewers for their valuable comments which helped to improve the manuscript.

## References

1 C. P. Byers, H. Zhang, D. F. Swearer, M. Yorulmaz, B. S. Hoener, D. Huang, A. Hoggard, W.-S. Chang, P. Mulvaney, E. Ringe, N. J. Halas, P. Nordlander, S. Link and C. F. Landes, From tunable core-shell nanoparticles to plasmonic drawbridges: Active control of nanoparticle optical properties, *Sci. Adv.*, 2015, **1**, e1500988.

2 M. Estrader, A. López-Ortega, S. Estradé, I. V. Golosovsky, G. Salazar-Alvarez, M. Vasilakaki, K. N. Trohidou, M. Varela, D. C. Stanley, M. Sinko, M. J. Pechan, D. J. Keavney, F. Peiró, S. Suriñach, M. D. Baró and J. Nogués, Robust antiferromagnetic coupling in hard-soft bi-magnetic core/shell nanoparticles, *Nat. Commun.*, 2013, **4**, 2960.

3 M. B. Gawande, A. Goswami, T. Asefa, H. Guo, A. V. Biradar, D.-L. Peng, R. Zboril and R. S. Varma, Core–shell nanoparticles: synthesis and applications in catalysis and electrocatalysis, *Chem. Soc. Rev.*, 2015, **44**, 7540–7590.

4 J.-H. Lee, J. Jang, J. Choi, S. H. Moon, S. Noh, J. Kim, J.-G. Kim, I.-S. Kim, K. I. Park and J. Cheon, Exchange-coupled magnetic nanoparticles for efficient heat induction, *Nat. Nanotechnol.*, 2011, **6**, 418–422.

5 E. J. Guidelli, O. Baffa and D. R. Clarke, Enhanced UV Emission From Silver/ZnO And Gold/ZnO Core-Shell Nanoparticles: Photoluminescence, Radioluminescence, And Optically Stimulated Luminescence, *Sci. Rep.*, 2015, **5**, 14004.

6 S. Song, X. Wang and H. Zhang, $CeO_2$-encapsulated noble metal nanocatalysts: enhanced activity and stability for catalytic application, *NPG Asia Mater.*, 2015, **7**, e179.

7 J. Wang and X. C. Zeng, Core–Shell Magnetic Nanoclusters, *Nanoscale Magn. Mater. Appl.*, 2009, 35–65.

8 A. Silva, rica Silva-Freitas, J. Carvalho, T. Pontes, R. Arajo-Neto, K. Silva, A. Carrio and E. Egito, in *Advances in Applied Biotechnology*, ed. M. Petre, InTech, 2012.

9 A. López-Ortega, M. Estrader, G. Salazar-Alvarez, A. G. Roca and J. Nogués, Applications of exchange coupled bi-magnetic hard/soft and soft/hard magnetic core/shell nanoparticles, *Phys. Rep.*, 2015, **553**, 1–32.

10 W. H. Meiklejohn and C. P. Bean, New Magnetic Anisotropy, *Phys. Rev.*, 1956, **102**, 1413–1414.

11 W. H. Meiklejohn and C. P. Bean, New Magnetic Anisotropy, *Phys. Rev.*, 1957, **105**, 904–913.

12 J. Nogués, J. Sort, V. Langlais, V. Skumryev, S. Suriñach, J. S. Muñoz and M. D. Baró, Exchange bias in nanostructures, *Phys. Rep.*, 2005, **422**, 65–117.

13 I. V. Golosovsky, G. Salazar-Alvarez, A. López-Ortega, M. A. González, J. Sort, M. Estrader, S. Suriñach, M. D. Baró and J. Nogués, Magnetic Proximity Effect Features in Antiferromagnetic/Ferrimagnetic Core-Shell Nanoparticles, *Phys. Rev. Lett.*, 2009, **102**, 247201.

14 M. Vasilakaki, K. N. Trohidou and J. Nogués, Enhanced Magnetic Properties in Antiferromagnetic-Core/Ferrimagnetic-Shell Nanoparticles, *Sci. Rep.*, 2015, **5**, 9609.

15 H. Ohldag, A. Scholl, F. Nolting, E. Arenholz, S. Maat, A. T. Young, M. Carey and J. Stöhr, Correlation between Exchange Bias and Pinned Interfacial Spins, *Phys. Rev. Lett.*, 2003, **91**, 017203.

16 W. Kuch, L. I. Chelaru, F. Offi, J. Wang, M. Kotsugi and J. Kirschner, Tuning the magnetic coupling across ultrathin antiferromagnetic films by controlling atomic-scale roughness, *Nat. Mater.*, 2006, **5**, 128–133.

17 A. Juhin, A. López-Ortega, M. Sikora, C. Carvallo, M. Estrader, S. Estradé, F. Peiró, M. D. Baró, P. Sainctavit and P. Glatzel, Direct evidence for an interdiffused intermediate layer in bi-magnetic core–shell nanoparticles, *Nanoscale*, 2014, **6**, 11911–11920.

18 W. Baaziz, B. P. Pichon, C. Lefevre, C. Ulhaq-Bouillet, J.-M. Greneche, M. Toumi, T. Mhiri and S. Bégin-Colin, High Exchange Bias in $Fe_{3-\delta}O_4$@CoO Core Shell Nanoparticles

Synthesized by a One-Pot Seed-Mediated Growth Method, *J. Phys. Chem. C*, 2013, **117**, 11436–11443.
19 N. Fontaíña Troitiño, B. Rivas-Murias, B. Rodríguez-González and V. Salgueiriño, Exchange Bias Effect in CoO@$Fe_3O_4$ Core–Shell Octahedron-Shaped Nanoparticles, *Chem. Mater.*, 2014, **26**, 5566–5575.
20 Z. Mao, X. Zhan and X. Chen, Defect-tuning exchange bias of ferromagnet/antiferromagnet core/shell nanoparticles by numerical study, *J. Phys. Condens. Matter*, 2012, **24**, 276002.
21 V. Dimitriadis, D. Kechrakos, O. Chubykalo-Fesenko and V. Tsiantos, Shape-dependent exchange bias effect in magnetic nanoparticles with core-shell morphology, *Phys. Rev. B*, 2015, **92**, 064420.
22 R. F. L. Evans, D. Bate, R. W. Chantrell, R. Yanes and O. Chubykalo-Fesenko, Influence of interfacial roughness on exchange bias in core-shell nanoparticles, *Phys. Rev. B*, 2011, **84**, 092404.
23 J. A. González, J. P. Andrés, R. López Antón, J. A. De Toro, P. S. Normile, P. Muñiz, J. M. Riveiro and J. Nogués, Maximizing Exchange Bias in Co/CoO Core/Shell Nanoparticles by Lattice Matching between the Shell and the Embedding Matrix, *Chem. Mater.*, 2017, **29**, 5200–5206.
24 E. Lottini, A. López-Ortega, G. Bertoni, S. Turner, M. Meledina, G. Van Tendeloo, C. de Julián Fernández and C. Sangregorio, Strongly Exchange Coupled Core|Shell Nanoparticles with High Magnetic Anisotropy: A Strategy toward Rare-Earth-Free Permanent Magnets, *Chem. Mater.*, 2016, **28**, 4214–4222.
25 N. Fontaíña-Troitiño, S. Liébana-Viñas, B. Rodríguez-González, Z.-A. Li, M. Spasova, M. Farle and V. Salgueiriño, Room-Temperature Ferromagnetism in Antiferromagnetic Cobalt Oxide Nanooctahedra, *Nano Lett.*, 2014, **14**, 640–647.
26 X. Deng, D. Yang, G. Tan, X. Li, J. Zhang, Q. Liu, H. Zhang, N. J. Mellors, D. Xue and Y. Peng, Bimagnetic h-Co/h-CoO nanotetrapods: preparation, nanoscale characterization, three-dimensional architecture and their magnetic properties, *Nanoscale*, 2014, **6**, 13710–13718.
27 P. Borisov, A. Hochstrat, X. Chen, W. Kleemann and C. Binek, Magnetoelectric Switching of Exchange Bias, *Phys. Rev. Lett.*, 2005, **94**, 117203.
28 S. Dey, M. D. Hossain, R. A. Mayanovic, R. Wirth and R. A. Gordon, Novel highly ordered core–shell nanoparticles, *J. Mater. Sci.*, 2017, **52**, 2066–2076.
29 M. d. Hossain, S. Dey, R. A. Mayanovic and M. Benamara, Structural and Magnetic Properties of Well-Ordered Inverted Core-Shell α-$Cr_2O_3$/α-$M_xCr_{2-x}O_3$ (M=Co, Ni, Mn, Fe) Nanoparticles, *MRS Adv.*, 2016, **FirstView**, 1–6.
30 M. D. Hossain, R. A. Mayanovic, R. Sakidja and M. Benamara, An experimental and theoretical study of the optical, electronic, and magnetic properties of novel inverted α-$Cr_2O_3$@α-$Mn_{0.35}Cr_{1.65}O_{2.94}$ core shell nanoparticles, *J. Mater. Res.*, 2017, **32**, 269–278.
31 B. Jamtveit, in *Growth, Dissolution and Pattern Formation in Geosystems*, eds. B. Jamtveit and P. Meakin, Springer Netherlands, 1999, pp. 65–84.
32 F. Farzaneh, Synthesis and Characterization of $Cr_2O_3$ Nanoparticles with Triethanolamine in Water under Microwave Irradiation, *J. Sci. Islam. Repub. Iran*, 2011, **22**, 329–333.
33 A. A. Coelho, Indexing of powder diffraction patterns by iterative use of singular value decomposition, *J. Appl. Crystallogr.*, 2003, **36**, 86–95.
34 C. A. Schneider, W. S. Rasband and K. W. Eliceiri, NIH Image to ImageJ: 25 years of image analysis, *Nat. Methods*, 2012, **9**, 671–675.
35 A. I. Liechtenstein, V. I. Anisimov and J. Zaanen, Density-functional theory and strong interactions: Orbital ordering in Mott-Hubbard insulators, *Phys. Rev. B*, 1995, **52**, R5467–R5470.
36 P. Giannozzi, S. Baroni, N. Bonini, M. Calandra, R. Car, C. Cavazzoni, Davide Ceresoli, G. L. Chiarotti, M. Cococcioni, I. Dabo, A. D. Corso, S. de Gironcoli, S. Fabris, G. Fratesi, R. Gebauer, U. Gerstmann, C. Gougoussis, Anton Kokalj, M. Lazzeri, L. Martin-Samos, N. Marzari, F. Mauri, R. Mazzarello, Stefano Paolini, A. Pasquarello, L. Paulatto, C. Sbraccia, S. Scandolo, G. Sclauzero, A. P. Seitsonen, A. Smogunov, P. Umari and R. M. Wentzcovitch, QUANTUM ESPRESSO: a modular and open-source software project for quantum simulations of materials, *J. Phys. Condens. Matter*, 2009, **21**, 395502.
37 H. Sawada, Residual electron density study of chromium sesquioxide by crystal structure and scattering factor refinement, *Mater. Res. Bull.*, 1994, **29**, 239–245.
38 H. J. Monkhorst and J. D. Pack, Special points for Brillouin-zone integrations, *Phys. Rev. B*, 1976, **13**, 5188–5192.
39 S. Shi, A. L. Wysocki and K. D. Belashchenko, Magnetism of chromia from first-principles calculations, *Phys. Rev. B*, 2009, **79**, 104404.
40 M. Cococcioni and S. de Gironcoli, Linear response approach to the calculation of the effective interaction parameters in the LDA+U method, *Phys. Rev. B*, 2005, **71**, 035105.
41 J. P. Perdew and A. Zunger, Self-interaction correction to density-functional approximations for many-electron systems, *Phys. Rev. B*, 1981, **23**, 5048–5079.
42 B. Silvi and A. Savin, Classification of chemical bonds based on topological analysis of electron localization functions, *Nature*, 1994, **371**, 683–686.
43 K. E. J. E. A. D. Becke, Becke, A. D. &amp; Edgecombe, K. E. A simple measure of electron localization in atomic and molecular systems. J. Chem. Phys. 92, 5397-5403, *J. Chem. Phys.*, 1990, **92**, 5397–5403.
44 K. Momma and F. Izumi, *VESTA 3* for three-dimensional visualization of crystal, volumetric and morphology data, *J. Appl. Crystallogr.*, 2011, **44**, 1272–1276.
45 J. Hu, H. Li, X. Huang and L. Chen, Improve the electrochemical performances of $Cr_2O_3$ anode for lithium ion batteries, *Solid State Ion.*, 2006, **177**, 2791–2799.

46 C.-H. Chen, M. R. Notis and D. B. Williams, Precipitation and Solid Solubility in the System NiO-$Cr_2O_3$, *J. Am. Ceram. Soc.*, 1983, **66**, 566–571.

47 H. Khurshid, S. Chandra, W. Li, M. H. Phan, G. C. Hadjipanayis, P. Mukherjee and H. Srikanth, Synthesis and magnetic properties of core/shell FeO/$Fe_3O_4$ nano-octopods, *J. Appl. Phys.*, 2013, **113**, 17B508.

48 H. Khurshid, W. Li, M.-H. Phan, P. Mukherjee, G. C. Hadjipanayis and H. Srikanth, Surface spin disorder and exchange-bias in hollow maghemite nanoparticles, *Appl. Phys. Lett.*, 2012, **101**, 022403.

49 S. Chandra, H. Khurshid, W. Li, G. C. Hadjipanayis, M. H. Phan and H. Srikanth, Spin dynamics and criteria for onset of exchange bias in superspin glass Fe/γ-$Fe_2O_3$ core-shell nanoparticles, *Phys. Rev. B*, 2012, **86**, 014426.

50 D. Tobia, E. Winkler, R. D. Zysler, M. Granada and H. E. Troiani, Size dependence of the magnetic properties of antiferromagnetic $Cr_2O_3$ nanoparticles, *Phys. Rev. B*, 2008, **78**, 104412.

51 X. Sun, N. Frey Huls, A. Sigdel and S. Sun, Tuning Exchange Bias in Core/Shell FeO/$Fe_3O_4$ Nanoparticles, *Nano Lett.*, 2012, **12**, 246–251.

52 A. E. Berkowitz, G. F. Rodriguez, J. I. Hong, K. An, T. Hyeon, N. Agarwal, D. J. Smith and E. E. Fullerton, Antiferromagnetic MnO nanoparticles with ferrimagnetic $Mn_3O_4$ shells: Doubly inverted core-shell system, Phys. Rev. B, 2008, **77**, 024403.

53 F. Maldonado, C. Novillo and A. Stashans, Ab initio calculation of chromium oxide containing Ti dopant, *Chem. Phys.*, 2012, **393**, 148–152.

54 H. Cao, X. Qiu, Y. Liang, M. Zhao and Q. Zhu, Sol-gel synthesis and photoluminescence of p-type semiconductor $Cr_2O_3$ nanowires, *Appl. Phys. Lett.*, 2006, **88**, 241112.

55 J. H. M Julkarnain, Optical properties of thermally evaporated $Cr_2O_3$ thin films, *Can. J. Chem. Eng. Amp Technol.*, 2012, **3**, 81–85.

56 M. M. Abdullah, F. M. Rajab and S. M. Al-Abbas, Structural and optical characterization of $Cr_2O_3$ nanostructures: Evaluation of its dielectric properties, *AIP Adv.*, 2014, **4**, 027121.

57 L. M. Corliss, J. M. Hastings, R. Nathans and G. Shirane, Magnetic Structure of $Cr_2O_3$, *J. Appl. Phys.*, 1965, **36**, 1099–1100.

58 R. Kubo, Electronic Properties of Metallic Fine Particles. I., *J. Phys. Soc. Jpn.*, 1962, **17**, 975–986.

59 A. K. Cheetham and D. A. O. Hope, Magnetic ordering and exchange effects in the antiferromagnetic solid solutions $Mn_xNi_{1-x}O$, *Phys. Rev. B*, 1983, **27**, 6964–6967.

60 W. Tang, E. Sanville and G. Henkelman, A grid-based Bader analysis algorithm without lattice bias, *J. Phys. Condens. Matter*, 2009, **21**, 084204.

61 E. Sanville, S. D. Kenny, R. Smith and G. Henkelman, Improved grid-based algorithm for Bader charge allocation, *J. Comput. Chem.*, 2007, **28**, 899–908.

62 S. Kumar, Y. J. Kim, B. H. Koo and C. G. Lee, Structural and magnetic properties of Ni doped $CeO_2$ nanoparticles, *J. Nanosci. Nanotechnol.*, 2010, **10**, 7204–7207.

63 M. D. Hossain, R. A. Mayanovic, R. Sakidja, M. Benamara and R. Wirth, Magnetic properties of core–shell nanoparticles possessing a novel Fe(II)-chromia phase: an experimental and theoretical approach, *Nanoscale*, 2018, **10**, 2138–2147.